energies

MDPI

Article

Different Features of Control Systems for Single-Phase Voltage Source Inverters

Zbigniew Rymarski * and Krzysztof Bernacki

Department of Electronics, Electrical Engineering and Microelectronics, Faculty of Automatic Control, Electronics and Computer Science, Silesian University of Technology, Akademicka 16, 44-100 Gliwice, Poland; krzysztof.bernacki@polsl.pl

* Correspondence: zrymarski@polsl.pl

Received: 23 July 2020; Accepted: 4 August 2020; Published: 7 August 2020

Abstract: The aim of this paper is to determine which type of control loop is better for each particular type of standard voltage source inverter (VSI) load (static, dynamic, nonlinear rectifier resistive-capacitive RC load). A comparison of three different types of controllers for single-phase VSIs is presented. The first two are of the single input single output (SISO)/proportional-integral-derivative controller (PID) and coefficient diagram method (CDM) types, and the third is of the multi-input single output (MISO)/passivity-based control (PBC) type. The selections of the gains for SISO and MISO controllers are presented, including the problem in the choice of PBC controller gains caused by the imperfection of the pulse width modulation (PWM) modulator. For a standard nonlinear rectifier RC load, the new control quality factor (CQF) is defined to distinguish the properties of the controllers. The results show the superiority of the MISO-PBC controller for the RC load; however, for a linear dynamic load, the MISO-PBC performed worse than the SISO-PID or CDM. Therefore, the choice between either a simple and inexpensive SISO with one measurement trace or an expensive MISO with three measurement traces depends on the purpose of the VSI. The initial simulations and measurements of the experimental models are presented and discussed.

Keywords: voltage source inverter; passivity-based control; control quality; nonlinear load; pulse width modulation; control systems; power conversion systems

1. Introduction

There are many different types of control systems that are used in voltage source inverters (VSIs) for uninterruptible power supply (UPS) systems. A serious problem is selecting the best control for dedicated applications. The solution can be a single input single output (SISO) system, in which only the output voltage is measured and controlled, while the output current is treated as an independent disturbance [1–3]. However, the output voltage has an influence on the output current, which creates an additional feedback loop. It is possible to calculate the shift of the poles of the characteristic equation of a closed-loop system when we consider this additional feedback loop and determine the final stability of an actual system [4,5]. The distortion of the input DC voltage of the inverter that results from operating different types of DC/DC converters (e.g., impedance networks that cooperate with photovoltaic (PV) modules) should also be considered [6,7]. The main advantage of an SISO solution is its simplicity and low cost because only one trace measuring output voltage with galvanic isolation is required. There have been some improvements to SISO using double control loops—a fast inner loop, e.g., a proportional-integral-derivative controller PID [8,9] or the coefficient diagram method (CDM) [10–12], and an outer loop that is only used to damp harmonic distortions, e.g., a repetitive controller (RPC) [13–18]. A repetitive controller is a discrete-time harmonic generator [14] that is plugged into the outer feedback loop, which works perfectly in the steady state

with a standard nonlinear RC load [19] while minimizing the output voltage static error (it damps the fundamental harmonic). However, it has one feature that can be a disadvantage for dynamic load changes: it remembers a disturbance from the previous fundamental cycle (the basic RPC has a register in which all of the previous fundamental cycle's values are stored) and even after the output disturbance vanishes, it still tries to damp it by distorting the output voltage. Therefore, a solution with an RPC cannot be compared with the fast multi-input instantaneous controllers. The inner feedback loop cooperates with the RPC best in the outer loop if its magnitude Bode plot is almost flat up to the Nyquist frequency.

A much more sophisticated system is a multi-input single output (MISO) system (Figure 1), in which the output current, the output filter inductor current, and the output voltage are measured and all of them are used as the input variables of the output voltage controller. In this case, the output current is also treated as a disturbance because the state-space matrix of the VSI does not depend on the particular load. However, in the case of MISO, we measure the output current (treated as a space variable or a measured disturbance [20]), which renders the problem of the missed feedback loop (output voltage—output current) unimportant.

The assignment of a linear or nonlinear plant model is the basic problem in control loop design. The inverter plant has some nonlinearity. The dead time T_{dt} of switching transistors in the H-bridge is one of the reasons for distortions of the output voltage [4] (a little step decrease in output voltage occurs when the inductor current changes direction) and can be taken into account in the nonlinear model of the inverter [21]. However, for the standard $T_{dt} \leq 0.5$ µs (for Metal-Oxide Semiconductor Field-Effect Transistors MOSFET, it can be tens of ns) and for the switching frequency $f_s = 20$ kHz (switching cycle $T_s = 50$ µs), the decrease in the fundamental harmonic of the output voltage is approximately only $T_{dt}/T_s \leq 1\%$. The problem of the influence of the nonlinear characteristic of the inductor in the inverter output filter on the design of the adaptive control loop (with calculation of the nonlinear inductance characteristic) is presented in [22]. However, the change in the coil's inductance and its equivalent serial resistance as a function of the amplitude and the frequency of its magnetizing current depends on the core material. For contemporary alloy-powder materials (e.g., Sendust (MS)/Super-MSS™ [23]), the exemplary change of inductance is about 5%, and the equivalent serial resistance is low in the operating point [24]. Therefore, it has no serious impact on the VSI model. The solution of the state-space equations of the pulse width modulation (PWM)-controlled VSI results in the nonlinear (exponential) dependency of the state-space variables on the switching on (duty) time [25]. In [26], the nonlinear control function is approximated by the Fourier series. The nonlinear modeling of the inverter using Hammerstein's approach (by means of the black-box identification method) is presented in [27]. All the approaches that take into account the nonlinearity of the inverter slightly increase the accuracy of its modeling; however, it has been shown that a linear approximation of VSI results in quite a satisfactory compatibility of the linear theory and the experimental model measurements and enables the easily understandable design of the control loop. Modeling the inverter as linear was practiced for many years (e.g., [1]) and resulted in the control design keeping low distortions of the output voltage for standard loads. We do not consider the thermal dependencies of the inductance, assuming that we work in standard ambient temperature conditions and that self-heating results in a stabilized temperature of the coil.

Estimating the quality of the VSI output voltage is also a challenge. The most common method for estimating static load distortions of the output voltage is to use the total harmonic distortion (THD) coefficient, which is simply the ratio of the root mean square (RMS) value of a set of the higher than the first harmonics of the output voltage to the RMS value of the fundamental harmonic. The problem is that this is an averaged value and the spectrum of harmonics cannot be discussed using it. The distortions of the VSI output voltage after dynamic load changes [19] are defined by means of the over- or undershoots of the output voltage and the settling time. There are some approaches that use wavelet analysis to present more complex distortions of the output voltage [28]. In systems with a discrete-time pulse width modulation (PWM) control, in which the delay of some (at least one)

switching cycles is unavoidable, the output voltage over- or undershoots are mainly the result of an insufficient capacitance in the VSI output filter (the feedback loop is important but to a lesser degree) because the system works in at least one switching period after the step decrease/increase in the load without control. For a sufficiently high output filter capacitance value, all of the properly designed SISO and MISO controllers reduced the distortions of the output voltage for the dynamic load to a similar degree. However, the settling time was different. Therefore, it seems that the most significant comparison of controller features can be done using a nonlinear RC load. A comparison of the distorted input inverter DC voltage in the case of the cooperation of a VSI with an impedance network for the discontinuous current mode (DCM) of a network was previously presented in [7]. Because the THD or the weighted THD (WTHD) [29] coefficients only show the averaged values, we will now analyze the spectrum of the harmonics of a single-phase VSI with selected control systems and attempt to determine which spectrum is the most appropriate for controlling a VSI. The newly defined control quality factor (CQF) will be used in order to permit a clear estimation of the SISO and MISO controller properties (Figure 1). Section 2 presents an analysis of the frequency range, in which the features of the controllers will be compared when considering the magnitude of the VSI output filter. Section 3 presents the approach to the discrete-time modeling of the VSI. Section 4 presents the exemplary SISO controllers of the VSI, and the MISO passivity-based control (PBC) PBC-IPBC2 is described in Section 5. Special attention was paid to selecting the PBC gains that were used in the simulations. Section 6 is devoted to a comparison of the SISO and MISO controllers for standard loads using an experimental VSI model. The main aim of the paper is to determine which type of control loop is more suitable for each particular type of standard load (static, dynamic, nonlinear rectifier RC load).

2. Analysis of the Frequency Range of the Controller Features

The transfer function of a simple continuous SISO model (Figure 1) of VSI (Figure 2) is calculated in Equation (1). Let us assume that in the steady state $V_{OUT} = V_{REF}$ and $k_V = 1$.

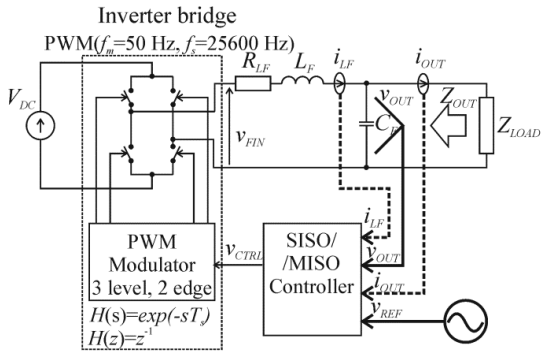

Figure 1. Single-phase voltage source inverter with single input single output (SISO) or multi-input single output (MISO) control.

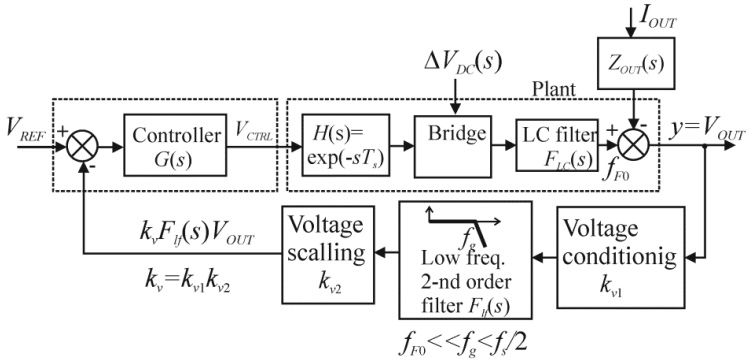

Figure 2. Simplified continuous SISO model of a voltage source inverter (VSI) with switching frequency f_s.

$$\begin{aligned} V_{OUT}(s) &= \frac{G(s)\exp(-sT_s)F_{LC}(s)}{1+k_vF_{lf}(s)G(s)\exp(-sT_s)F_{LC}(s)}V_{REF}(s) \\ &+\frac{MF_{LC}(s)}{1+k_vF_{lf}(s)G(s)\exp(-sT_s)F_{LC}(s)}\Delta V_{DC}(s)+ \\ &+\frac{-Z_{OUT}(s)}{1+k_vF_{lf}(s)G(s)\exp(-sT_s)F_{LC}(s)}I_{OUT}(s) \end{aligned} \quad (1)$$

In the simplified continuous model (Figure 2), for $T_s << T_m$ (switching period T_s, fundamental period T_m), we can omit the delay, $\exp(-sT_s)$, of the PWM modulator (Figure 1). The transfer function of the changes ΔV_{DC} in the V_{DC} voltage supplying the VSI can decrease the result of the distortion of the DC voltage from the impedance network [6,7]. The output impedance of the VSI without a feedback loop Z_{OUT} is calculated in Equation (2), where R_{LF} is an equivalent serial parasitic resistance of the VSI bridge and the filter choke. In further calculations, we will assign $k_V = 1$.

$$Z_{OUT}(j\omega) = \frac{R_{LF}+j\omega L_F}{(1-\omega^2L_FC_F)+j\omega C_FR_{LF}} \quad (2)$$

We neglect the equivalent serial resistance (ESR) R_{CF} of the capacitor C_F. There is a problem with estimating the damping coefficient ζ_F when a load current is modeled as an independent current source. Therefore, the damping coefficient ζ_F will be calculated in Equation (3) for a case in which the nominal load resistance R_{LOAD} is present in the transfer function of the VSI. For $R_{LF} << R_{LOAD}$, the output filter transfer function is calculated in Equation (3),

$$F_{LC}(j\omega) \approx \frac{1}{(1-\omega^2/\omega_{F0}{}^2)+j2\xi_F\omega^2/\omega_{F0}{}^2}, \text{ where } \omega_{F0} = \frac{1}{\sqrt{L_FC_F}}, \ \xi_F = \frac{1}{2}(R_{LF}\sqrt{\frac{C_F}{L_F}}+\frac{1}{R_{LOAD}}\sqrt{\frac{L_F}{C_F}}) \quad (3)$$

For the low-frequency range below ω_{F0} (the resonant frequency of the output filter L_FC_F), the output impedance of the VSIs without feedback loop Z_{OUT}, the transfer functions F_{LC}, and F_{lf} (Figure 2) are calculated in Equation (4),

$$Z_{OUT}(j\omega)\big|_{\omega<<\omega_{F0}} \approx R_{LF}+j\omega L_F, \ F_{LC}(j\omega)\big|_{\omega<<\omega_{F0}} \approx 1, \ F_{lf}(j\omega)\big|_{\omega<<\omega_{F0}} \approx 1 \quad (4)$$

The transfer function of the output current, which is treated as an independent disturbance for the low-frequency range, lower than ω_{F0} is calculated in Equation (5),

$$\left.\frac{V_{OUT}(j\omega)}{I_{OUT}(j\omega)}\right|_{\omega<<\omega_{F0}} \approx -\frac{(R_{LF}+j\omega L_F)}{G(j\omega)} \quad (5)$$

The transfer function of DC voltage change ΔV_{DC} for the low-frequency range $\omega << \omega_{F0}$ and $k_V = 1$ is calculated in Equation (6),

$$\left.\frac{V_{OUT}(j\omega)}{\Delta V_{DC}(j\omega)}\right|_{\omega<<\omega_{F0}} \approx \frac{M}{G(j\omega)} \quad (6)$$

The specific case shown in Equation (7) is for $\omega = \omega_{F0}$, and the values of $L_F = 1$ mH, $C_F = 50$ µF, and $R_{LF} < 1$ were used.

$$Z_{OUT}(j\omega)\big|_{\omega=\omega_{F0}} \approx \frac{1}{R_{LF}}\frac{L_F}{C_F}, F_{LC}(j\omega)\big|_{\omega=\omega_{F0}} \approx \frac{1}{j2\xi_F}, \ \left.\frac{V_{OUT}(j\omega)}{I_{OUT}(j\omega)}\right|_{\omega=\omega_{F0}} \approx \frac{1}{R_{LF}}\frac{L_F}{C_F}\frac{1}{jG(j\omega_{F0})/(2\xi_F)-1} \quad (7)$$

The transfer function of ΔV_{DC} for the low-frequency range $\omega = \omega_{F0}$ and $k_V = 1$ is calculated in Equation (8),

$$\left.\frac{V_{OUT}(j\omega)}{\Delta V_{DC}(j\omega)}\right|_{\omega=\omega_{F0}} \approx \frac{M}{j2\xi_F+G(j\omega_{F0})} \quad (8)$$

For the high-frequency range over ω_{F0}, the output impedance Z_{OUT} of the VSI without the feedback loop and the transfer function of the output current (which is treated as an independent disturbance) for the high-frequency range over ω_{F0} is calculated in Equation (9). We assume that filter $F_{LC}(j\omega)$ for $\omega >> \omega_{F0}$ damps the signals of whatever is the transfer function $F_{lf}(j\omega)$ ($|F_{lf}(j\omega)| \leq 1$).

$$Z_{OUT}(j\omega)\Big|_{\omega>>\omega_{F0}} \approx \frac{1}{j\omega C_F},\ F_{LC}(j\omega)\Big|_{\omega>>\omega_{F0}} \approx -\frac{{\omega_{F0}}^2}{\omega^2},\ \frac{V_{OUT}(j\omega)}{I_{OUT}(j\omega)}\Bigg|_{\omega>>\omega_{F0}} = -\frac{1}{j\omega C_F}. \tag{9}$$

The transfer function of ΔV_{DC} for the high-frequency range $\omega >> \omega_{F0}$ and $k_V = 1$ is calculated in Equation (10),

$$\frac{V_{OUT}(j\omega)}{\Delta V_{DC}(j\omega)}\Bigg|_{\omega>>\omega_{F0}} \approx -M\frac{{\omega_{F0}}^2}{\omega^2} \tag{10}$$

Equations (9) and (10) mean that for $\omega >> \omega_{F0}$, the output impedance of the VSI with the feedback loop and the transfer function of ΔV_{DC} with the feedback loop are not dependent on it.

It can be seen from the presented Equations (1)–(10) that the gain of the controller is important in damping the disturbances for the resonant frequency ω_{F0} and below this frequency of the output filter. For the higher frequencies, it is not important because of the high suppression of the output filter. This discussion, which is based on Figure 2, led to the further investigation of controller properties being carried out in the $2\omega_{F0}$ frequency range.

3. Discrete-Time Modeling of the Voltage Source Inverter

Today, only the digital control of VSI is important. Every PWM discrete-time modulator implements one switching period delay T_s (the data are written for the modulator in one switching cycle, and the pulse width is set in the next cycle). For VSIs that are used in UPS systems, the requirement of low output voltage harmonics has made the sinusoidal PWM the most popular. In the case of a single-phase VSI with a four-transistor, three-level H-bridge, a double-edge PWM is usually a sufficient solution. The design of the discrete-time controller requires that a discrete-time or continuous model of a VSI be used. The first approach is based on the continuous to discrete-time transformation (the discretized plant) using the zero order hold (ZOH) model or the Tustin model [4,30]. The second approach is based on solving the state-space equations (the discrete plant) and linearizing the control function [1,21,30]. The third approach is based on the continuous model of a VSI, adjusting the quasi-continuous-time counterpart of the discrete-time controller, and finally, using a discrete-time controller (the discretized controller) [8,9]. The first and third solutions are based on the averaged models. The second solution considers the PWM features that distinguish the single and double-edge PWM. However, for a relatively high switching frequency, all of them gave similar results of control. The state variables $\mathbf{x} = [v_{OUT}\ i_{LF}\ i_{OUT}]^T$, the control (input) variable u = v_{FIN}, the output variable y = v_{OUT} (Figure 1), and the state A and control B matrixes were calculated in Equation (11) when the ESR of the capacitor was neglected. The state-space equations $\dot{x} = Ax + Bu$ were solved for the time period of the switching on T_{ONk} ($V_{FIN} = V_{DC}$) and switching off T_{OFFk} ($V_{FIN} = 0$). However, we obtained nonlinear equations for the control, so the discrete-time control matrix G_D was approximated $\exp(AT_{ONk}/2) \approx I + AT_{ONk}/2$ to linearize them [1,16,25]. Finally, the discrete-time state-space equations were obtained, as shown in Equations (11)–(15) [4,21,30].

$$A = \begin{bmatrix} 0 & \frac{1}{C_F} & -\frac{1}{C_F} \\ -\frac{1}{L_F} & -\frac{R_{LF}}{L_F} & 0 \\ 0 & 0 & 0 \end{bmatrix}, B = \begin{bmatrix} 0 \\ \frac{1}{L_F} \\ 0 \end{bmatrix} \tag{11}$$

$$x_{k+1} = A_D x_k + G_D T_{ONk} \tag{12}$$

$$A_D = e^{AT_s} = \Phi(T_s) = L^{-1}\left[(sI - A)^{-1}\right]\Big|_{t\,=\,T_s} \tag{13}$$

$$G_D = e^{AT_s/2}BV_{DC} = \Phi(T_s/2)BV_{DC} \tag{14}$$

$$A_D = \Phi(T_s) = \begin{bmatrix} \phi_{11} & \phi_{12} & \phi_{13} \\ \phi_{21} & \phi_{22} & \phi_{23} \\ \phi_{31} & \phi_{32} & \phi_{33} \end{bmatrix}, G_D = \begin{bmatrix} g_{11} \\ g_{21} \\ g_{31} \end{bmatrix} \tag{15}$$

Where

$$\begin{array}{l} \xi_F = \frac{1}{2}R_{LF}\sqrt{C_F/L_F} \\ \phi_{11} = [\cos(\omega_{F0}T_s) + \xi_F \sin(\omega_{F0}T_s)]\exp(-\xi_F\omega_{F0}T_s), \\ \phi_{12} = \frac{1}{\omega_{F0}C_F}\sin(\omega_{F0}T_s)\exp(-\xi_F\omega_{F0}T_s),\ \varphi_{13} = -\varphi_{12} + R_{LF}(\varphi_{11} - 1), \\ \phi_{21} = -\frac{C_F}{L_F}\varphi_{12},\ \phi_{22} = [\cos(\omega_{F0}T_s) - \xi_F \sin(\omega_{F0}T_s)]\exp(-\xi_F\omega_{F0}T_s),\ \phi_{23} = 1 - \varphi_{11}, \\ \phi_{31} = 0,\ \phi_{32} = 0,\ \phi_{33} = 1 g_{11} = V_{DC}\omega_{F0}\sin(\omega_{F0}\frac{T_s}{2})\exp(-\xi_F\omega_{F0}\frac{T_s}{2}), \\ g_{21} = \frac{V_{DC}}{L_F}\left[\cos(\omega_{F0}\frac{T_s}{2}) - \xi_F \sin(\omega_{F0}\frac{T_s}{2})\right]\exp(-\xi_F\omega_{F0}\frac{T_s}{2}),\ g_{31} = 0 \end{array} \tag{16}$$

The damping ζ_F calculated from the space Equation (14) was not dependent on the load Z_{LOAD} (Figure 1) because if I_{OUT} was treated as an independent current source (Figure 2), the load was absent in the space equations. This is the difference in the Equations (16) and (3) describing ζ_F value.

The output voltage discrete-time transfer function for the open loop is a control function of the duty cycle, which is controlled by v_{CTRL} and a function ($-Z_{OUT}$, where Z_{OUT} is an output impedance) of the output current Equation (17). The discrete-time control transfer function of a VSI Equation (24) considers an additional delay of one T_s of the discrete-time modulator $H(z)$.

$$V_{OUT}(z) = z^{-1}\frac{T_s}{V_{DC}}G_{inv}V_{CTRL}(z) - Z_{OUT}(z)I_O(z) \tag{17}$$

For the open-loop system, Equations (18) and (19) are used:

$$K_{VSI} = \frac{V_{OUT}(z)}{V_{CTRL}(z)} = z^{-1}\frac{T_s}{V_{DC}}G_{inv} = \frac{\frac{T_s}{V_{DC}}g_{11}z^{-2} + \frac{T_s}{V_{DC}}(\varphi_{12}g_{21} - \varphi_{22}g_{11})z^{-3}}{1 - (\varphi_{11} + \varphi_{22})z^{-1} + (\varphi_{11}\varphi_{22} - \varphi_{12}\varphi_{21})z^{-2}} \tag{18}$$

$$Z_{OUT}(z) = \frac{\varphi_{13}z^{-1} + (\varphi_{12}\varphi_{23} - \varphi_{13}\varphi_{22})z^{-2}}{1 - (\varphi_{11} + \varphi_{22})z^{-1} + (\varphi_{11}\varphi_{22} - \varphi_{12}\varphi_{21})z^{-2}} \tag{19}$$

Similar results of the discrete-time model for a VSI can be achieved using the c2d MATLAB function with the simplest ZOH discretization [30] or the discretization in the analytic way [8,9].

4. SISO Control of a VSI

The first presented example of an SISO control is a modern discretized PID controller (presented in detail in [8,9]), which uses the simplest SISO model from Figure 2 but includes an R_{LOAD}. The quasi-continuous transfer function [8,9] of the plant $K_p(s)$ (including R_{LOAD}), considering a further ZOH discretization and one T_s delay of the modulator, is shown in Equation (20),

$$K_p(s) = \exp(-s\frac{T_s}{2})\exp(-sT_s)F_{LC}(s) \approx (1 - s\frac{T_s}{2})\frac{1 - s\frac{T_s}{2}}{1 + s\frac{T_s}{2}}\frac{{\omega_{F0}}^2}{s^2 + 2\xi_F\omega_{F0}s + (1 + \frac{R_{LF}}{R_{LOAD}})\omega_{F0}{}^2} \tag{20}$$

The discrete-time PID controller is as in Equation (21),

$$C\left(z^{-1}\right) = \frac{b_0 + b_1z^{-1} + b_2z^{-2}}{1 - z^{-1}} \tag{21}$$

The difference control law for $k_V = 1$ is as in Equation (22),

$$\begin{array}{c} v_{CTRL}(k) = v_{CTRL}(k-1) + b_0(v_{OUT}(k) - v_{REF}(k)) \\ +b_1(v_{OUT}(k-1) - v_{REF}(k-1)) + b_2(v_{OUT}(k-2) - v_{REF}(k-2)) \end{array} \quad (22)$$

For the experimental model: $T_s = 1/f_s = 1/2{,}5600$ s, $L_F = 1$ mH, $C_F = 50$ µF, $R_{LF} = 1\ \Omega$, $R_{LOAD} = 50\ \Omega$; the PID controller transfer function from [8] will be $b_0 = 18.014$, $b_1 = 33.495$, $b_2 = 16.094$. These coefficients were analyzed based on the root locus [8]. In Reference [9], these coefficients were slightly adjusted: $b_0 = 18.381$, $b_1 = 34.179$, $b_2 = 16.423$.

A more sophisticated SISO system is presented in Figure 3 [10,11,31,32].

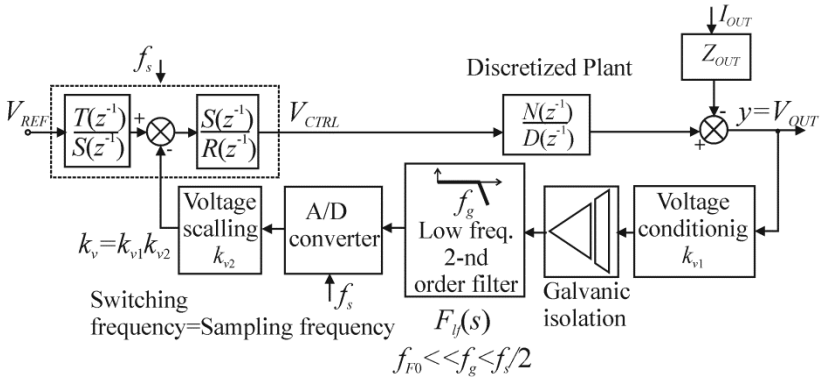

Figure 3. An advanced discretized SISO system.

The concept of a Manabe CDM [10–12,31] design of the controller (T, S, R) is such that the coefficients of the closed-loop characteristic polynomial have assumed values, in the simplest case, of Standard Manabe Form. For $k_v = 1$ (v_{REF} is properly scaled), the output voltage of a closed-loop system is as in Equation (23),

$$v_{OUT}\left(z^{-1}\right) = \frac{TN}{RD + SN} v_{REF}\left(z^{-1}\right) - \frac{Z_{OUT}RD}{RD + SN} I_{OUT}\left(z^{-1}\right) \quad (23)$$

The characteristic equation of a closed-loop system is as in Equation (24),

$$P\left(z^{-1}\right) = R\left(z^{-1}\right)D\left(z^{-1}\right) + S\left(z^{-1}\right)N\left(z^{-1}\right) = \sum_{i=0}^{n} p_{zi} z^{-i} \quad (24)$$

From Equation (18), Equation (25) can be derived:

$$K_{VSI} = \frac{N\left(z^{-1}\right)}{D(z^{-1})} = \frac{a_2 z^{-2} + a_3 z^{-3}}{1 + b_1 z^{-1} + b_2 z^{-2}} \quad (25)$$

For a system with a disturbance (in our case I_{OUT}), the degrees of R and S are equal to or higher than $n-1$, where n is the degree of D. In our case, we will assume Equation (26):

$$S\left(z^{-1}\right) = \sum_{i=0}^{2} s_i z^{-i},\ R\left(z^{-1}\right) = \sum_{i=0}^{2} r_i z^{-i},\ r_0 = 1 \quad (26)$$

The Diophantine Equation (27) should be solved for $r_0 = p_0 = 1$.

$$\left(1 + r_1 z^{-1} + r_2 z^{-2}\right)\left(1 + b_1 z^{-1} + b_2 z^{-2}\right) + \left(s_0 + s_1 z^{-1} + s_2 z^{-2}\right)\left(a_2 z^{-2} + a_3 z^{-3}\right) = \sum_{i=0}^{5} p_{zi} z^{-1} \quad (27)$$

To solve Equation (27), Equation (28) should be solved to obtain the r_i and s_i coefficients,

$$\begin{bmatrix} 1 & 0 & 0 & 0 & 0 \\ b_1 & 1 & a_2 & 0 & 0 \\ b_2 & b_1 & a_3 & a_2 & 0 \\ 0 & b_2 & 0 & a_3 & a_2 \\ 0 & 0 & 0 & 0 & a_3 \end{bmatrix} \begin{bmatrix} r_1 \\ r_2 \\ s_0 \\ s_1 \\ s_2 \end{bmatrix} = \begin{bmatrix} p_{z1} - b_1 \\ p_{z2} - b_2 \\ p_{z3} \\ p_{z4} \\ p_{z5} \end{bmatrix} \tag{28}$$

where Equation (29),

$$a_2 = \frac{T_s}{V_{DC}} g_{11},\ a_3 = \frac{T_s}{V_{DC}} (\varphi_{12} g_{21} - \varphi_{22} g_{11}),\ b_1 = -(\varphi_{11} + \varphi_{22}),\ b_2 = \varphi_{11}\varphi_{22} - \varphi_{12}\varphi_{21} \tag{29}$$

The coefficients p_i of Standard Manabe Form in a continuous system for the 5th degree of $P(s)$ are the following:

$$p_0(s^0) = 1,\ p_1(s^1) = p_0\tau,\ p_2(s^2) = 0.4\, p_0\tau^2,\ p_3(s^3) = 0.08\, p_0\tau^3,\ p_4(s^4) = 0.008\, p_0\tau^4,\ p_5(s^5) = 0.0004\, p_0\tau^5,$$

where τ is the time constant of a closed-loop system. Satisfactory results of the control of the experimental model were achieved for $\tau = 4\ T_s$ and for $\tau = 5\ T_s$.

Let us define the following discrete-time transfer function using the *c2d* function with the discretization cycle T_s = 1/2.5600 s and the default ZOH method Equation (30) [4]:

$$K(z) = c2d(\frac{1}{\sum_{i=0}^{5} p_i(s) s^i}, T_s) = \frac{\sum_{i=0}^{5} w_i(z) z^{-i}}{\sum_{i=0}^{5} p_{zi}(z^{-1}) z^{-i}} \tag{30}$$

For $\tau = 4\ T_s$:

$p_{z0}(z^0) = 1$, $p_{z1}(z^{-1}) = -1.327$, $p_{z2}(z^{-2}) = 0.6811$, $p_{z3}(z^{-3}) = -0.1826$, $p_{z4}(z^{-4}) = 0.0381$, $p_{z5}(z^{-5}) = -0.006738$.

This last calculation enables $v_{OUT} = v_{REF}$ to be kept in the steady state Equation (31).

$$t_0 = \frac{P(z = 1)}{N(z = 1)} = \frac{V_{DC}}{T_s} \frac{1 + p_{z1} + p_{z2} + p_{z3} + p_{z4} + p_{z5}}{\varphi_{12} g_{21} + (1 - \varphi_{22}) g_{11}} \tag{31}$$

For the experimental model, the solutions of Equations (28) and (31) were:

$r_0 = 1$, $r_1 = 0.5898$, $r_2 = 0.4218$, $s_0 = 29.5050$, $s_1 = -24.2037$, $s_2 = -0.4607$, $t_0/V_{DC} = 0.1713$.

However, in many cases t_0 is adjusted individually. The difference control law for $k_v = 1$ is as in Equation (32),

$$v_{CTRL}(k) = -r_1 v_{CTRL}(k-1) - r_2 v_{CTRL}(k-2) + t_0 v_{REF} - s_0 v_{OUT}(k) - s_1 v_{OUT}(k-1) - s_2 v_{OUT}(k-2) \tag{32}$$

5. MISO Control of VSI

MISO controllers with multiple controller inputs, i.e., the output voltage, filter inductor current, and output current, and a single output, i.e., voltage (Figure 1), effectively reduce the distortions of the output voltage for the different types of loads that are defined in [19]. One of the MISO controls that is described often lately is the passivity-based control (PBC) presented by Ortega [33] in 1989. PBC seems to be one of the best solutions for power conversion systems such as VSIs [20,34–36]. A VSI is presented as an energy transformation multiport device [37]. If the stored energy is less than the supplied energy, the system is passive. The "injection" of the appropriate damping [34] is basic for the control of the inductor and output currents; however, in the so-called improved PBC [34], there is direct feedback from the output voltage. The state variables that define the energy of the VSI are defined

as in Equations (33) and (34). The output current, which does not exist in the function of the system energy, is treated as an independent disturbance [20].

$$x = \begin{bmatrix} L_F i_{LF} & C_F v_{OUT} \end{bmatrix}^T = P\begin{bmatrix} i_{LF} & v_{OUT} \end{bmatrix}^T \tag{33}$$

$$P = \begin{bmatrix} L_F & 0 \\ 0 & C_F \end{bmatrix}, P^{-1} = \begin{bmatrix} 1/L_F & 0 \\ 0 & 1/C_F \end{bmatrix} \tag{34}$$

The total energy that is stored in the system is described by the Hamiltonian function $H(x)$ in Equations (35) and (36),

$$H(x) = \frac{1}{2}\left(L_F {i_{LF}}^2 + C_F {v_{OUT}}^2\right) = \frac{1}{2}x^T P^{-1} x \tag{35}$$

$$\begin{bmatrix} i_{LF} & v_{OUT} \end{bmatrix}^T = P^{-1}x = \partial H(x)/\partial(x) \tag{36}$$

The error vector $\boldsymbol{e}$ is defined as Equations (37)–(39),

$$e = \begin{bmatrix} L_F\left(i_{LF} - i_{LFref}\right) \\ C_F\left(v_{OUT} - v_{OUTref}\right) \end{bmatrix} = P\begin{bmatrix} i_{LF} - i_{LFref} \\ v_{OUT} - v_{OUTref} \end{bmatrix} \tag{37}$$

$$H(e) = \frac{1}{2}\left(L_F\left(i_{LF} - i_{LFref}\right)^2 + C_F\left(v_{OUT} - v_{OUTref}\right)^2\right) = \frac{1}{2}e^T P^{-1} e \tag{38}$$

$$\begin{bmatrix} i_{LF} - i_{LFref} \\ v_{OUT} - v_{OUTref} \end{bmatrix} = P^{-1}e = \partial H(e)/\partial e \tag{39}$$

v_{OUTref} is the reference, sinusoidal output voltage waveform;

i_{LFref} is the calculated reference current of the inductor.

The equilibrium of a closed-loop system is asymptotically stable [38] and is achieved if $H(e)$ has a minimum in $\boldsymbol{x} = \mathrm{x}_{ref}$ in Equation (40),

$$\left.\frac{\partial H(e)}{\partial x}\right|_{x\,=\,x_{ref}} = 0, \left.\frac{\partial^2 H(e)}{\partial x^2}\right|_{x\,=\,x_{ref}} > 0 \tag{40}$$

The system is passive if the time derivative $H(e)$ is negative in Equation (41),

$$\frac{\mathrm{d}H(e)}{\mathrm{d}t} < 0 \tag{41}$$

Two equations are used—the first for a closed-loop system Equation (42) [20] and the second for an open-loop system, as in Equation (43),

$$\dot{e} = [J - (R + R_a)]P^{-1}e \tag{42}$$

$$\dot{x} = [J - R]P^{-1}x + \begin{bmatrix} V_{DC} \\ 0 \end{bmatrix}m + \begin{bmatrix} 0 \\ -1 \end{bmatrix}i_{OUT} \tag{43}$$

where the interconnection matrix, J, and the damping matrix, R, can be defined as in Equation (44),

$$J = \begin{bmatrix} 0 & -1 \\ 1 & 0 \end{bmatrix}, R = \begin{bmatrix} R_{LF} & 0 \\ 0 & 0 \end{bmatrix} \tag{44}$$

R_a (the PBC controller) is the matrix Equation (45) of the injected damping, R_i is the gain of the current error, and K_v is the conductive gain of the voltage error.

$$R_a = \begin{bmatrix} R_i & 0 \\ 0 & K_v \end{bmatrix} \tag{45}$$

Subtracting Equation (42) from Equation (43) results in the control law Equation (46),

$$\dot{e} - \dot{x} = [J - R]P^{-1}(e - x) - R_a P^{-1} e - \begin{bmatrix} V_{DC} \\ 0 \end{bmatrix} m - \begin{bmatrix} 0 \\ -1 \end{bmatrix} i_{OUT} \tag{46}$$

For $v_{CTRL} = mV_{DC}$, the difference control law of a single-phase VSI with a PBC is shown in Equations (47) and (48),

$$v_{CTRL}(k) = -R_i i_{LF}(k) + (R_i + R_{LF}) i_{LFref}(k) + L_F \frac{i_{LFref}(k) - i_{LFref}(k-1)}{T_c} + v_{OUTref}(k) \tag{47}$$

$$i_{LFref}(k) = K_v \left[v_{OUTref}(k) - v_{OUT}(k) \right] + C_F \frac{v_{OUTref}(k) - v_{OUTref}(k-1)}{T_c} + i_{OUT}(k) \tag{48}$$

The inductor current is an integral of a function of the output voltage, which is important for the steady-state error in the control law. The adjustment of the PBC gains, R_i and K_v, is a problem. The matrix $R + R_a$ should be positively defined to fill this requirement Equation (41) [20]. In practice, this means that $R_i + R_{LF}$ and K_v should be positive. Calculating the upper restrictions of their values can be difficult [34]. The higher their values are, the higher the convergence of the error tracking is. The characteristic polynomial of a closed-loop system with a PBC is shown in Equation (49),

$$\det\left\{ [J - (R + R_a)]P^{-1} - \lambda 1 \right\} = \begin{bmatrix} (-R_{LF} - R_i)1/L_F - \lambda & -1/C_F \\ 1/L_F & (-K_v)1/C_F - \lambda \end{bmatrix} \tag{49}$$

The roots $\lambda_{1,2}$ Equation (50) of the characteristic polynomial Equation (49) of a closed-loop system Equation (42) will always have the real part negative (Figure 4a,b) for the positively defined $R + R_a$ matrix.

$$\lambda_{1,2} = \frac{\left\{ -[(R_{LF} + R_i)C_F + L_F K_V] \pm \sqrt{[(R_{LF} + R_i)C_F + L_F K_v]^2 - 4L_F C_F [1 + (R_{LF} + R_i)K_v]} \right\}}{2L_F C_F} \tag{50}$$

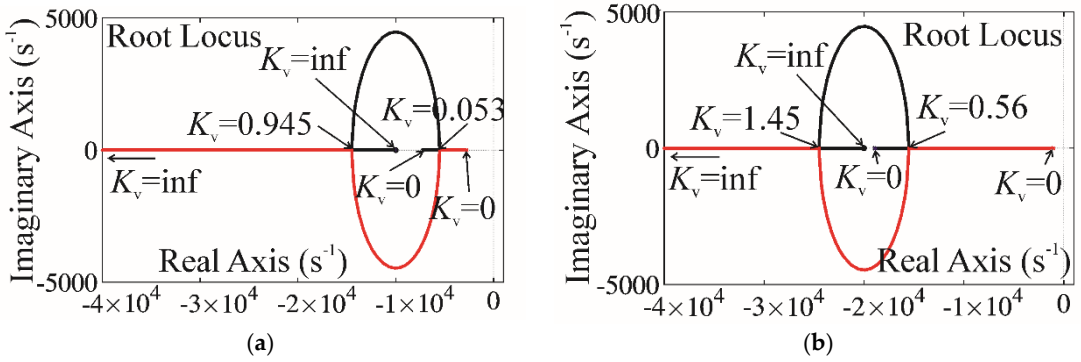

Figure 4. The root locus of the characteristic polynomial of a closed-loop system with passivity-based control (PBC) for L_F = 1 mH, C_F = 50 µF: (**a**) $R_{LF} + R_i$ = 10 Ω, (**b**) $R_{LF} + R_i$ = 20 Ω.

However, in the simulations and in the experimental model, overly high values of R_i and K_v led to oscillations in the control voltage and output voltage (Figure 5). An overly high value of modulation index M [39,40] for the nonlinear rectifier RC load led to the saturation of the PWM modulator (Figure 6). Both of these cases produced the same result. The reason can be the disability of fast current changing in the filter inductor [40]. Therefore, the best adjustment of the PBC controller gains R_i and K_v is to determine the lowest THD (for the nonlinear rectifier RC load).

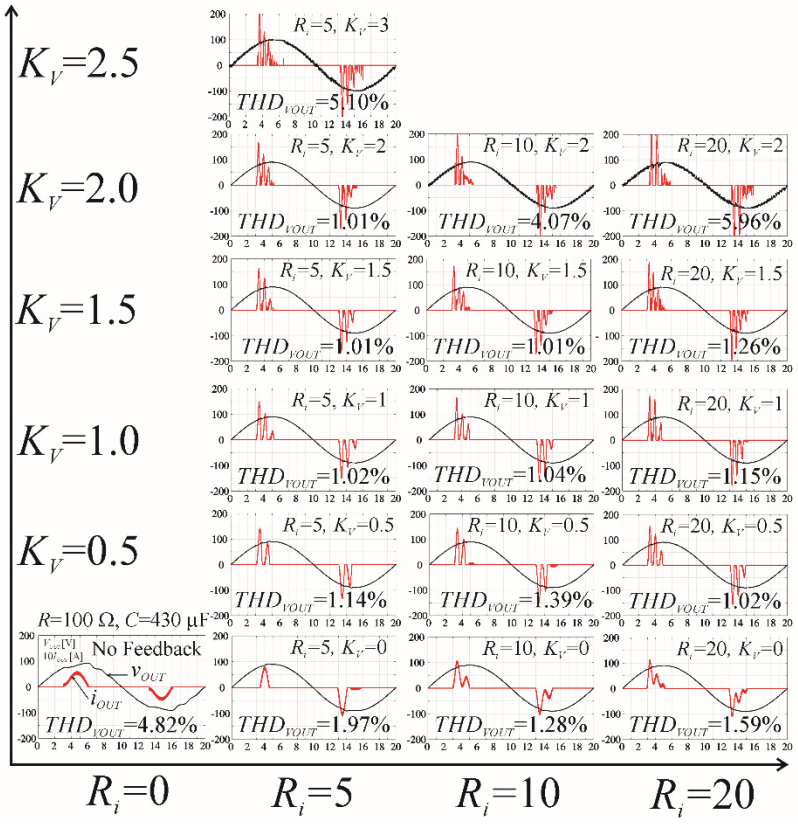

Figure 5. The simulation of the output voltage and current waveforms for rectifier R = 100 Ω and C = 430 μF for M = 0.3 and different values of R_i and K_V.

Figure 6 presents two problems. The first is saturation in the PWM modulator due to overly high values of the PBC gains (R_i and K_V). The second case can be presented comparing the root loci from Figure 4a,b and Figure 6. For R_i = 10, oscillations can occur for K_V = 0–1, for R_i = 20, and for K_V = 0.5–1.5. The second problem was not so important. The value of M = 0.3 was too low in practice. It was experimentally checked in the VSI model and finally set at M = 0.8, R_i = 5, and K_V = 0.5. The equations from the literature did not solve the problem of restricting the upper R_i and K_V values. From Figure 5, it is obvious that an MISO control with a low M value is able to efficiently control the output current. The presented PBC control was further named IPBC2 because compared to the basic PBC theory [34], it used the output voltage as in [34] and its derivative in the final control law. This derivative was absent in the improved PBC (IPBC) that was presented in [34].

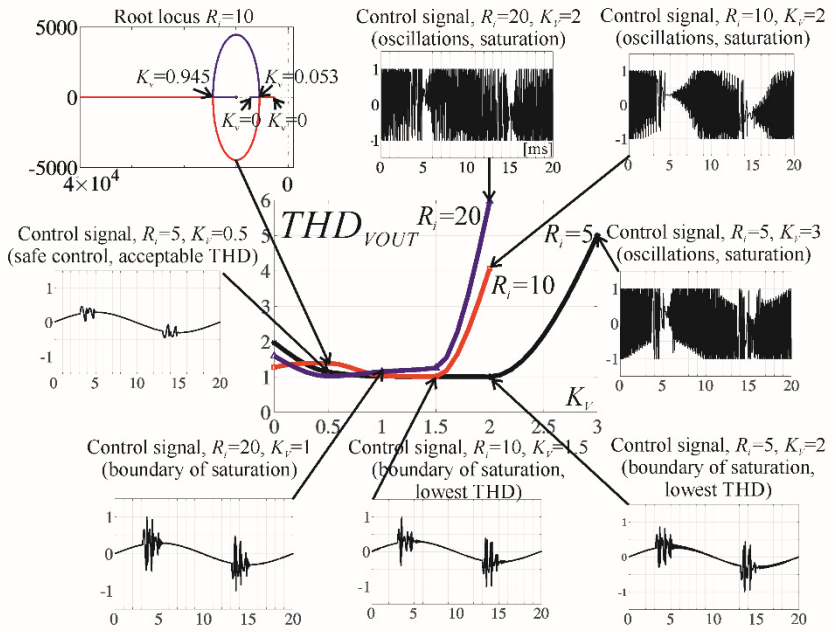

Figure 6. The adjustment of the R_i and K_v gains of the PBC (simulation) for M = 0.3.

The idea of the calculation of the upper limit of R_i gain was presented in [34]. The derivative of the control voltage v_{CTRL} in one switching cycle should be lower than the maximum carrier slope in the PWM modulator. For the double-edge modulation and recalculating it to the DC voltage level, it is equal to $V_{DC}/(T_s/2)$ [34]. However, it is shown in Figures 5 and 6 that the mutual dependency of the two PBC controller gains is very important. In one sampling period, we can assume $\mathrm{d}(v_{OUTref})/\mathrm{d}t \approx 0$. Therefore, from Equation (48) we can calculate:

$$i_{LFref}(kT_s) = (\frac{1}{R_{LOAD}} - K_v)v_{OUT}(kT_s) + v_{OUTref}(kT_s) \tag{51}$$

$$\frac{di_{LFREF}(kT_s)}{dt} \approx (\frac{1}{R_{LOAD}} - K_v)\frac{dv_{OUT}(kT_s)}{dt} \tag{52}$$

From Equations (47), (51) and (52), we can calculate Equation (53):

$$\begin{array}{c}\frac{dv_{CTRL}(kT_s)}{dt} \approx L_F(\frac{1}{R_{LOAD}} - K_v)\frac{d^2v_{OUT}(kT_s)}{dt^2} \\ +(R_i + R_{LFe})(\frac{1}{R_{LOAD}} - K_v)\frac{dv_{OUT}(kT_s)}{dt} - R_i\frac{di_{LF}(kT_s)}{dt}\end{array} \tag{53}$$

In one switching cycle, for $R_{LOAD} = \infty$, we can assume Equation (54):

$$\left.\frac{di_{LF}(kT_s)}{dt}\right|_{\max,\min} \approx \pm\frac{V_{DC}}{L_F},\ \left.\frac{dv_{OUT}(kT_s)}{dt}\right|_{\max} \approx \frac{i_{LF}}{C_F},\ \left.\frac{d^2v_{OUT}(kT_s)}{dt^2}\right|_{\max} \approx \left.\frac{d}{dt}\left(\frac{i_{LF}}{C_F}\right)\right|_{\max} \approx \pm\frac{V_{DC}}{L_FC_F} \tag{54}$$

$$\left.\frac{dv_{CTRL}(kT_s)}{dt}\right|_{\max} \approx K_v[L_F + (R_i + R_{LFe})T_s]\frac{V_{DC}}{L_FC_F} + R_i\frac{V_{DC}}{L_F} \tag{55}$$

The final restriction of PBC gains, R_i and K_v, from Equation (55) is Equation (56),

$$K_v[L_F + (R_i + R_{LFe})T_s]\frac{1}{C_F} + R_i < \frac{2L_F}{T_s} \tag{56}$$

The restrictions of the operating area, shown in Figure 7, can be one of the reasons for the THD increase in the higher values of PBC gains presented in Figures 5 and 6. However, Equation (56) does

not consider the modulation index M value because the maximum carrier slope does not depend on M (the reference voltage depends on M). Equation (56) is calculated for $R_{LOAD} = \infty$, while the restrictions of the K_v value for the existing load resistance will be slightly lower.

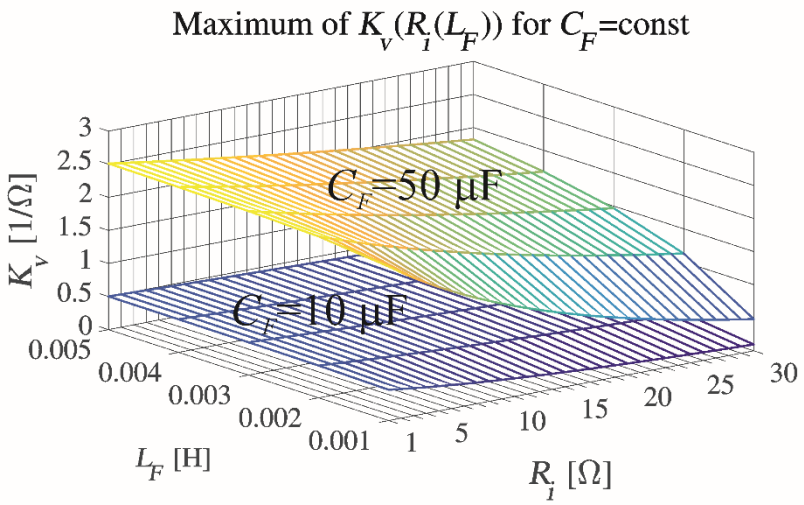

Figure 7. The restrictions (worst case) of the maximum K_v gain due to the R_i gain in the function of L_F, for the constant C_F to keep the derivative of the control voltage below the maximum carrier slope in the PWM modulator for L_F = 1–5 mH, C_F = 10 and 50 μF, R_{LF} = 1 Ω and $R_{LOAD} = \infty$, according to Equation (56).

6. Comparison of Experimental Voltage Source Inverters with PID, CDM, and PBC Control Systems

The comparison of the SISO-PID (the version from [8,9]), SISO-CDM, and MISO-PBC-IPBC2 systems was based on measurements of the VSI output voltage for standard loads. Figure 8a–d presents the output voltage for the standard [19] nonlinear rectifier RC load for R = 100 Ω and C = 430 μF. The vertical axis of Figure 8a–d is scaled in units of the 13th bit bipolar Analog To Digital Converter ADC. The actual voltage amplitude was about 60 V. The output filter (L_F = 1 mH, C_F = 50 μF) resonant frequency was about 712 Hz. The initial analysis (Section 2) showed that the feedback loop is only important for the neighborhood of this frequency (about 14th harmonic) and below. Therefore, a sufficient frequency range for comparing the controllers was from the 2nd up to the 30th harmonic. Figure 8a–d presents the output voltage waveforms without feedback and with the PID, CDM, and PBC-IPBC2 controllers. The THD coefficient was calculated for each case. The PID and CDM controllers had similar THD, while for the PBC, it was a bit lower. However, the output voltage waveforms were different. The harmonics spectra are presented in Figure 9a–d. It can be noticed that the harmonics spectrum is different for the different controllers. Some of the harmonics are increased (e.g., the 2nd harmonic for the CDM controller increased because the voltage waveform was not ideally symmetrical). The importance of a decrease or increase in a specific harmonic was dependent on its relative amplitude. Therefore, the influence of the feedback loop on the particular harmonic can be defined as in Equation (57),

$$x_n = h_{NFBn} 20 \log_{10} \frac{h_{NFBn}}{h_{CTRLn}} \quad (57)$$

where h_{NFBn} is the n-th relative harmonic amplitude of the output voltage without feedback and h_{CTRLn} is the n-th relative harmonic using the selected controller. The sum of the x_n values is a measure of the

feedback quality. The better the quality, the higher the value of the coefficient. Therefore, the final definition of the control quality factor (*CQF*) is as in Equation (58),

$$CQF = \sum_{1}^{n} h_{NFBn} 20 \log_{10} \frac{h_{NFBn}}{h_{CTRLn}} \tag{58}$$

where m is the harmonic order above the filter resonant frequency, in our case $m = 30$.

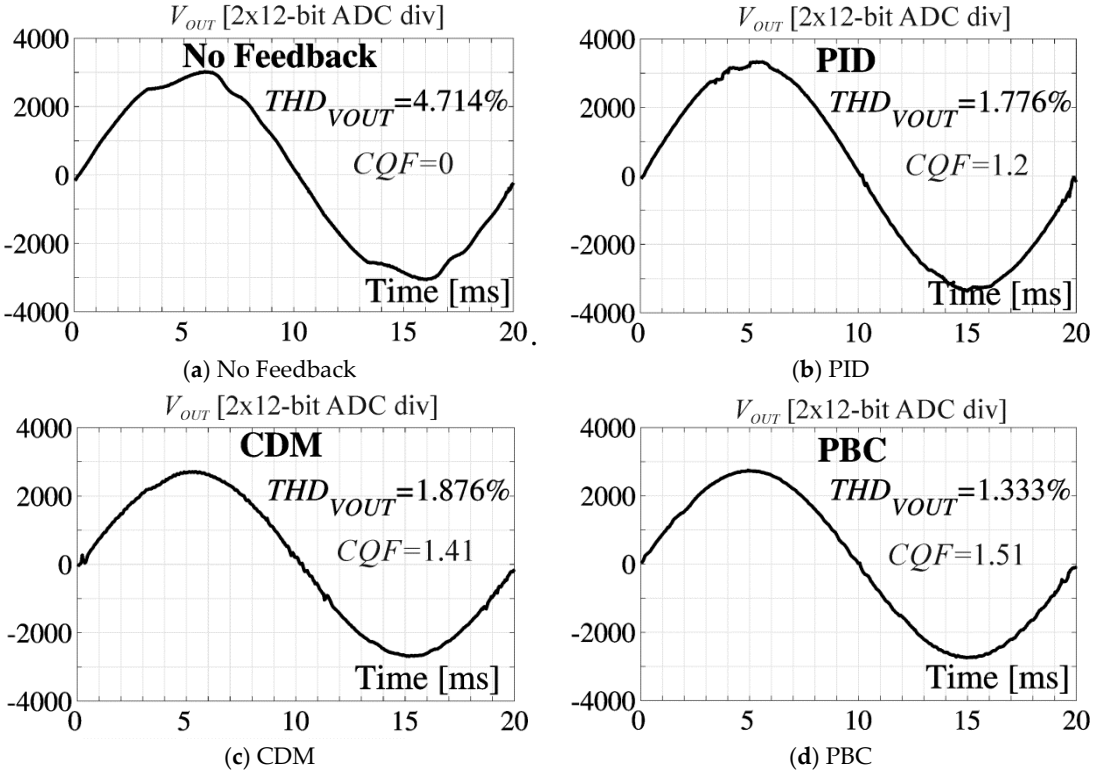

Figure 8. Measured VSI output voltage for the different types of control systems for the standard RC load, (**a**) without the feedback loop; (**b**) the SISO-PID controller; (**c**) the SISO-CDM controller; (**d**) the MISO-PBC-IPBC2 controller

The higher the *CQF*, the better the control. It can be seen from Figure 8a–d that for the nonlinear rectifier RC load, the best controller was the PBC (*CQF* = 1.51), the second best was the CDM (*CQF* = 1.41), and the third best was the PID (*CQF* = 1.2). The *CQF* measure enabled us to distinguish the quality of PID and CDM controls that had almost the same THD. The nonlinear load caused harmonic disturbances, and the *CQF* was the proper measure of their damping.

The quality of the control should also be determined for a dynamic load change. Figure 10a–d shows the over-and undershoots after a dynamic load decrease and increase (45 Ω to 500 Ω and 500 Ω to 45 Ω) and the settling time. The lowest over- and undershoots (about 3% and −2%) were for the CDM control, the shortest settling time (about 1 ms in both cases) was for the PID control, and the worst parameters were for the PBC-IPBC2 (about 6% and −5.1%, 3.5 and 2 ms). It would be difficult to improve the dynamic properties of the PBC because increasing the gains R_i and K_V would lead to higher oscillations and a longer settling time, while decreasing them would lead to higher over- and undershoots. In the PBC, we directly control the filter inductor current as in Equations (47) and (48) but the inductance disables fast current changes, which can lead to the saturation of the modulator. The capacitance in the output filter has a significant influence on the over- and undershoots.

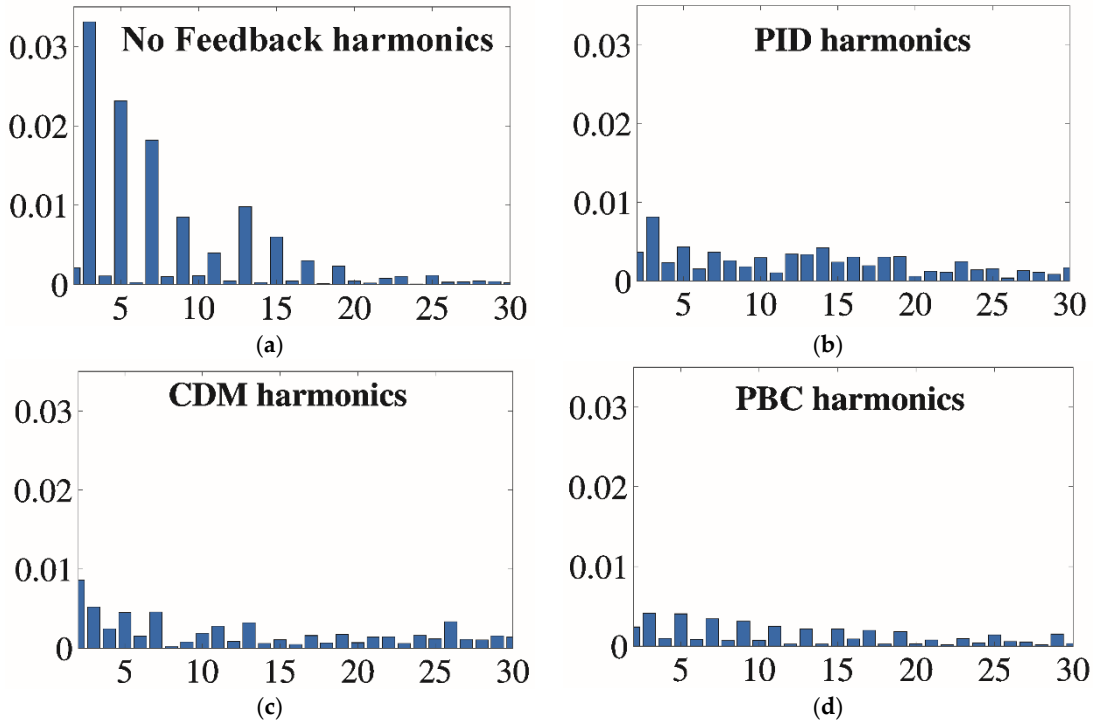

Figure 9. Measured harmonics spectrum of the different types of control systems, (**a**) without the feedback loop; (**b**) the SISO-PID controller; (**c**) the SISO-CDM controller; (**d**) the MISO-PBC-IPBC2 controller.

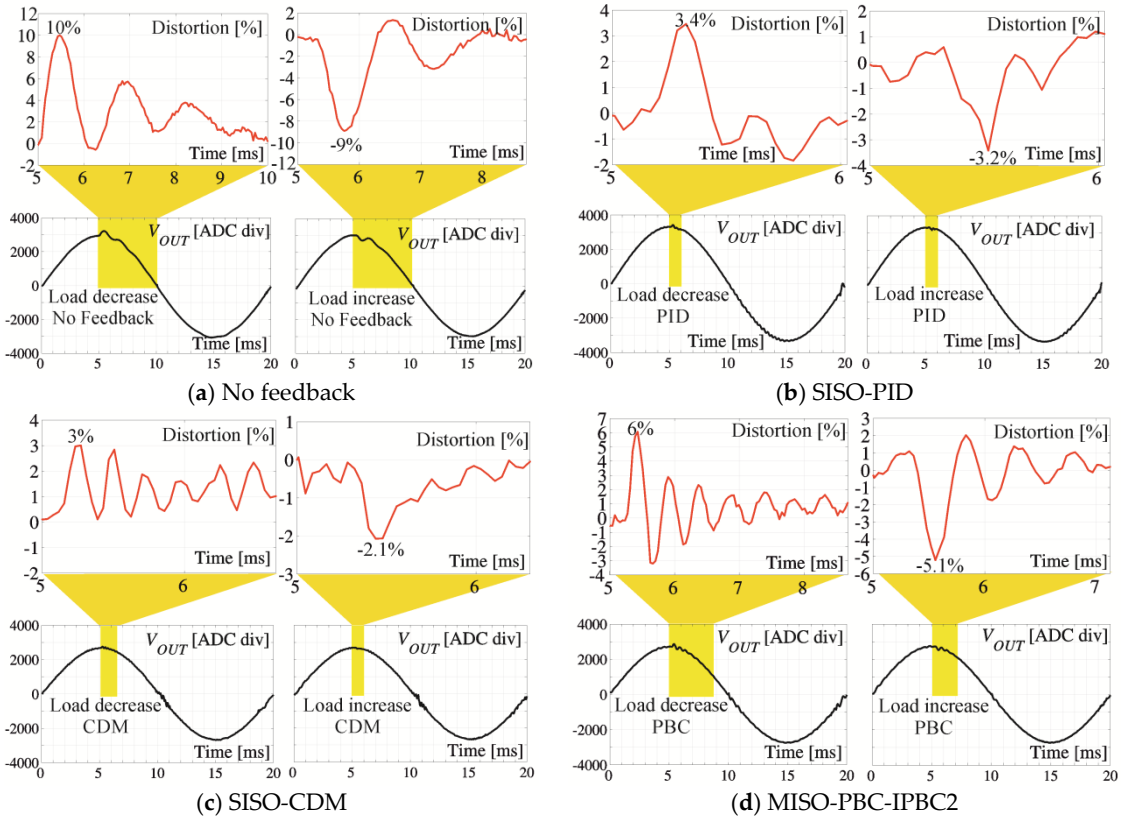

Figure 10. The over- and undershoots after a decrease and increase in the dynamic load (45 Ω to 500 Ω and 500 Ω to 45 Ω) and the settling time, (**a**) without the feedback loop; (**b**) the SISO-PID controller; (**c**) the SISO-CDM controller; (**d**) the MISO-PBC-IPBC2 controller.

7. Materials and Methods

The presented simulations were performed using MATLAB-Simulink for the VSI model with L_F = 1 mH, R_{LF} = 1 Ω, C_F = 50 μF and the switching frequency f_s = 25,600 Hz (Figures 5–7). The modulation index in simulations was M = 0.3. The first PWM scheme [41,42] of 3-level modulation was used. The VSI experimental model had the same nominal parameter values as the MATLAB model except that the modulation index was M = 0.8. The filter coil core was made of Super-MSS™ material [23,42], and the output capacitor was of the Metallized Polypropylene Capacitor MKP type. The transistor switches of the H-bridge were International Rectifier HEXFETs - IRFP 360, which have R_{DS}(on) = 0.20 Ω (@10 A). The PID [8,9], CDM, and IPBC2 control laws were programmed in an STM32F405VG microcontroller by means of Keil μVision C++. The static load resistance varied from 50 to 2000 Ω, and the dynamic load resistance was a step load from 50||500 to 500 Ω and from 500 Ω to 50||500. The nonlinear rectifier RC load was for R = 100 Ω and C = 430 μF. The amplitude of the experimental VSI output voltage was 60 V, and the values of the voltages in Figures 8 and 10 are presented in units of the ADC converter (the −4093 to 4093 range). The waveforms (two fundamental periods) were transmitted from the inverter model to the PC with the visualization software (Figure 11), then computed and plotted using MATLAB (Figures 8 and 10).

Figure 11. The experimental VSI model and PC with dedicated visualization software.

8. Results

The results of the measurements of the VSI experimental model are presented in Table 1. With the inclusion of the new CQF factor, an increase in the resolution of the estimation of the three different controls' results should be enabled. We can use simple and cheap SISO-PID or SISO-CDM controllers (without the filter coil current and the VSI output current sensors) in the case of the static and dynamic linear loads of the VSI. However, in the case of the nonlinear rectifier RC load, a better solution is MISO-IPBC2. The restrictions of the K_v and R_i gains in the MISO-IPBC2 (Figures 5–7) complicate its further improvement. The requirement of the restriction of the product of the modulation index M and the filter inductor value L_F (the higher the L_F, the lower the M) is a problem that exists for all the controller types and was described, e.g., in [39,40].

Table 1. Parameters of the VSI output voltage with standard loads for the different controllers.

Type of Control	No Feedback	SISO-PID	SISO-CDM	MISO-PBC-IPBC2
Rectifier RC load (R = 100 Ω, C = 430 μF)	THD = 4.714%	THD = 1.78% CQF = 1.2	THD = 1.88% CQF = 1.41	THD = 1.33% CQF = 1.51
Load decrease (45 Ω to 500 Ω)	ΔV_{OUT} = 10% Settling: 4 ms	ΔV_{OUT} = 3.4% Settling: 1 ms	ΔV_{OUT} = 3.0% Settling: 1.5 ms	ΔV_{OUT} = 6% Settling: 3.5 ms
Load increase (500 Ω to 45 Ω)	ΔV_{OUT} = −9% Settling: 3.5 ms	ΔV_{OUT} = −3.2% Settling: 1 ms	ΔV_{OUT} = −2.1% Settling: 1.2 ms	ΔV_{OUT} = −5.1% Settling: 2 ms
Static error of the amplitude (500 Ω to 45 Ω)	4%	2%	2%	2%

9. Conclusions

A comparison of SISO-PID, SISO-CDM, and MISO-PBC-IPBC2 systems showed that for the nonlinear rectifier RC load defined in the IEC 62040-3 standard [19], the best results (the lowest distortions of the output voltage) were for the PBC-IPBC2 controller that had the gains adjusted after the initial simulations (Figures 5–7). The measurement of the currents enabled them to be better shaped (Figure 5). A new control quality factor was defined and enabled a better resolution in the description of the control results. An analysis of the root locus (Figure 4a,b) showed that the voltage source inverter with the PBC-IPBC2 control should always be stable for any positive gains R_i and K_V; however, the simulations (Figures 5–7) and measurements of the experimental model showed that oscillations in the output voltage existed for the higher values of gains. It is obvious that the MISO-PBC-IPBC2 system with the output current and filter inductor current measurements better damped the important harmonics (Figure 9a–d). The output voltage parameters (the over- and undershoots, the settling time) for the linear dynamic load were worse for the PBC-IPBC2, and we were not able to improve them by changing the values of the controller gains. An increase in the gains decreased the over- and undershoots but increased the settling time because of oscillations. The reason for the worse dynamic response of the PBC could be the direct control the filter inductor current, during which the inductance disables fast current changes, which can lead to the saturation of the modulator [40]. The static error, which was calculated as the decrease in output voltage amplitude after an increase in the load (500 to 45 Ω), was low and was similar for all of the controllers (about 2% vs. 4% without feedback), which is understandable because the static error was mainly reduced by the integration action of the output voltage. All of the controllers had such an action (the PBC-IPBC2 controller due to the control of the inductor current, which was dependent on the integration of the function of the VSI output voltage). All of the controllers cause small oscillations (Figure 10a–d) in the VSI output voltage (in the experimental model) close to the zero crossing, which could have been the result of the wind up effect of the controller (the voltage error was integrated, and the three-level PWM for the voltage crossing zero was not able to control the output voltage efficiently with very short pulses). To summarize, in the case of a nonlinear load, the more expensive MISO-PBC-IPBC2 controller had much lower distortions of the VSI output voltage, while in the case of dynamic loads, the less expensive SISO-PID and SISO-CDM controllers were sufficient and the static error was the same for all the controllers. Therefore, the final selection of either a simple and inexpensive SISO with one measurement trace or an expensive MISO with three measurement traces depends on the proposed function of the VSI.

Author Contributions: Conceptualization, Z.R. and K.B.; methodology, Z.R. and K.B.; software, Z.R.; validation, Z.R., and K.B.; formal analysis, Z.R. and K.B.; investigation, Z.R. and K.B.; resources, Z.R. and K.B.; writing—original draft preparation, Z.R.; writing—review and editing, Z.R. and K.B.; visualization, Z.R.; supervision, Z.R.; project administration, Z.R. and K.B.; funding acquisition, Z.R. and K.B. All authors have read and agreed to the published version of the manuscript.

Funding: This research was partially supported by the Polish Ministry of Science and Higher Education funding for statutory activities (BK-284/RAU11/2020). Authors were supported by the Polish National Centre for Research and Development, grant no. TANGO3/427467/NCBR/2019.

Acknowledgments: The calculations were performed using IT infrastructure that was funded by the GeCONiI project (POIG.02.03.01-24-099/13).

Conflicts of Interest: The authors declare no conflict of interest.

References

1. Kawamura, A.; Chuarayapratip, R.; Haneyoshi, T. Deadbeat control of PWM inverter with modified pulse patterns for uninterruptible power supply. *IEEE Trans. Ind. Electron.* **1988**, *35*, 295–300. [CrossRef]
2. Kusko, A.; Galler, D.; Medora, N. Output impedance of PWM UPS inverter-feedback vs. filters. In *Conference Record of the 1990 IEEE Industry Applications Society Annual Meeting, 7–12 October*; Institute of Electrical and Electronics Engineers: New York, NY, USA, 1990; Volume 2. [CrossRef]
3. Deng, H.; Srinivasan, D.; Oruganti, R. Modeling and control of single-phase UPS inverters: A survey. In Proceedings of the International Conference on Power Electronics and Drives Systems, PEDS 2005, Kuala Lumpur, Malaysia, 28 November–1 December 2005; Volume 2, pp. 848–853. [CrossRef]
4. Rymarski, Z. Design Method of Single-Phase Inverters for UPS Systems. *Int. J. Electron.* **2009**, *96*, 521–535. [CrossRef]
5. Rymarski, Z. The influence of the output filter parameters tolerance and the load on the PID/CDM control of the single phase VSI. *Przegląd Elektrotechniczny* **2011**, *87*, 114–117.
6. Rymarski, Z.; Bernacki, K. Drawbacks of impedance networks. *Int. J. Circuit Theory Appl.* **2018**, *46*, 612–628. [CrossRef]
7. Rymarski, Z.; Bernacki, K.; Dyga, Ł. Decreasing the single phase inverter output voltage distortions caused by impedance networks. *IEEE Trans. Ind. Appl.* **2019**, *55*, 7586–7594. [CrossRef]
8. Blachuta, M.; Rymarski, Z.; Bieda, R.; Bernacki, K.; Grygiel, R. Design, Modeling and Simulation of PID Control for DC/AC Inverters. In Proceedings of the 24th International Conference on Methods and Models in Automation and Robotics, Międzyzdroje, Poland, 26–29 August 2019; pp. 428–433. [CrossRef]
9. Blachuta, M.; Rymarski, Z.; Bieda, R.; Bernacki, K.; Grygiel, R. In Proceedings of the Continuous-time approach to discrete-time PID Control for UPS inverters—A case study. In Proceedings of the Asian Conference on Intelligent Information and Database Systems, ACIIDS, Phuket, Thailand, 23–26 March 2020; pp. 1–12.
10. Manabe, S. Coefficient diagram method. *IFAC Proc. Vol.* **1998**, *31*, 211–222. [CrossRef]
11. Manabe, S. Importance of coefficient diagram in polynomial method. In Proceedings of the 42nd IEEE Conference on Decision and Control, Maui, HI, USA, 9–12 December 2003; pp. 3489–3494. [CrossRef]
12. Coelho, J.P.; Pinho, T.M.; Boaventura-Cunha, J. Controller system design using the coefficient diagram method. *Arab. J. Sci. Eng.* **2016**, *41*, 3663–3681. [CrossRef]
13. Tomizuka, M.; Tsao, T.C.; Chew, K.K. Analysis and synthesis of discrete-time repetitive controllers. *Asme J. Dyn. Syst. Meas. Control* **1989**, *111*, 353–358. [CrossRef]
14. Luo, F.L.; Ye, H.; Rashid, M. *Digital Power Electronics and Applications*; Elsevier Academic Press: Cambridge, MA, USA, 2006. [CrossRef]
15. Gangling, Z.; Guan, M.; Wang, Y. Application of repetitive control for aeronautical static inverter. In Proceedings of the 2007 2nd IEEE Conference on Industrial Electronics and Applications, ICIEA, Harbin, China, 23–25 May 2007; pp. 121–125. [CrossRef]
16. Rech, C.; Pinheiro, H.; Gründling, H.A.; Hey, H.L.; Pinheiro, J.R. Comparison of digital control techniques with repetitive integral action for low cost PWM inverters. *IEEE Trans. Power Electron.* **2003**, *18*, 401–410. [CrossRef]
17. Lidozzi, A.; Ji, C.; Solero, L.; Crescimbini, F.; Zanchetta, P. Load-adaptive zero-phase-shift direct repetitive control for stand-alone four-leg VSI. *IEEE Trans. Ind. Appl.* **2016**, *52*, 4899–4908. [CrossRef]
18. Liu, Z.; Zhang, B.; Zhou, K.; Yang, Y.; Wang, J. Virtual variable sampling repetitive control of single-phase DC/AC PWM converters. *IEEE J. Emerg. Sel. Top. Power Electron.* **2019**, *7*, 1837–1845. [CrossRef]
19. IEC 62040-3:2011. Uninterruptible Power Systems (UPS)-Part 3: Method of Specifying the Performance and Test Requirements. Available online: https://webstore.iec.ch/publication/6344 (accessed on 21 July 2020).

20. Serra, F.M.; De Angelo, C.H.; Forchetti, D.G. IDA-PBC control of a DC–AC converter for sinusoidal three-phase voltage generation. *Int. J. Electron.* **2017**, *104*, 93–110. [CrossRef]
21. Xie, R.; Hao, X.; Yang, X.; Chen, W.; Huang, L.; Wang, C. An exact discrete-time model considering dead-time nonlinearity for an H-bridge grid-connected inverter. In Proceedings of the 2014 International Power Electronics Conference (IPEC-Hiroshima 2014—ECCE ASIA), Hiroshima, Japan, 8–12 May 2014; pp. 2950–2953. [CrossRef]
22. Yuan, W.; Wang, Y.; Liu, D.; Deng, F.; Chen, Z. Robust droop control of ac microgrid against nonlinear characteristic of inductor. In Proceedings of the IEEE 10th International Symposium on Power Electronics for Distributed Generation Systems (PEDG), Xi'an, China, 3–6 June 2019; pp. 642–647. [CrossRef]
23. 2019 Alloy Powder Products Catalog, Micrometals Powder Core Solutions. Available online: https://www.micrometals.com/design-and-applications/literature/ (accessed on 21 July 2020).
24. Bernacki, K.; Rymarski, Z.; Dyga, Ł. Selecting the coil core powder material for the output filter of a voltage source inverter. *Electron. Lett.* **2017**, *53*, 1068–1069. [CrossRef]
25. Rymarski, Z. The discrete model of the power stage of the voltage source inverter for UPS. *Int. J. Electron.* **2011**, *98*, 1291–1304. [CrossRef]
26. Cheng, X.; Chen, Y.; Chen, X.; Zhang, B.; Qiu, D. An extended analytical approach for obtaining the steady-state periodic solutions of SPWM single-phase inverters. In Proceedings of the IEEE Energy Conversion Congress and Exposition (ECCE), Cincinnati, OH, USA, 24 August 2017; pp. 1311–1316. [CrossRef]
27. Cheng, Y.; Zha, X.; Liu, Y. Nonlinear modeling of inverter using the Hammerstein's approach. In Proceedings of the INTELEC 2009—31st International Telecommunications Energy Conference, Incheon, Korea, 18–22 October 2009; pp. 1–4. [CrossRef]
28. Dyga, Ł.; Rymarski, Z.; Bernacki, K. The wavelet-aided methods for evaluating the output signal that is designated for uninterruptible power supply systems. *Przegląd Elektrotechniczny* **2020**. accepted paper.
29. van der Broeck, H.W. Analytical calculation of the harmonic effects of single phase multilevel PWM inverters. In Proceedings of the 29th Annual Conference of the IEEE Industrial Electronics Society IECON, 2–6 November 2003; pp. 243–248. [CrossRef]
30. Rymarski, Z.; Bernacki, K. Different approaches to modelling single-phase voltage source inverters for uninterruptible power supply systems. *IET Power Electron.* **2016**, *9*, 1513–1520. [CrossRef]
31. Hamamci, S.E.; Kaya, I.; Koksal, M. Improving performance for a class of processes using coefficient diagram method. In Proceedings of the 9th Mediterranean Conference on Control and Automation, MED'01, Dubrovnik, Croatia, 27–29 June 2001; pp. 1–6.
32. Astrom, K.J.; Wittenmark, B. *Computer-Controlled Systems: Theory and Design*, 3rd ed.; Dover Publications Inc.: Upper Saddle River, NJ, USA; Mineola, NY, USA, 2011.
33. Ortega, R.M.; Spong, M.W. Adaptive motion control of rigid robots: A tutorial. *Automatica* **1989**, *25*, 877–888. [CrossRef]
34. Komurcugil, H. Improved passivity-based control method and its robustness analysis for single-phase uninterruptible power supply inverters. *IET Power Electron.* **2015**, *8*, 1558–1570. [CrossRef]
35. Gui, Y.; Wei, B.; Li, M.; Guerrero, J.M.; Vasquez, J.C. Passivity-based coordinated control for islanded AC microgrid. *Appl. Energy* **2018**, *229*, 551–561. [CrossRef]
36. Meshram, R.V.; Bhagwat, M.; Khade, S.; Wagh, S.R.; Aleksandar, M.; Stankovic, A.M.; Singh, N.M. Port-controlled phasor hamiltonian modeling and IDA-PBC control of solid-state transformer. *IEEE Trans. Control Syst. Technol.* **2019**, *27*, 161–174. [CrossRef]
37. Hill, D.; Zhao, J.; Gregg, R.; Ortega, R. *20 Years of Passivity–Based Control (PBC): Theory and Applications*; CDC Workshop: Shanghai, China, 15 December 2009.
38. Wang, Z.; Goldsmith, P. Modified energy-balancing-based control for the tracking problem. *IET Control Theory Appl.* **2008**, *2*, 310–312. [CrossRef]
39. Rymarski, Z. The analysis of output voltage distortion minimization in the 3-phase VSI for the nonlinear rectifier RoCo. *Przegląd Elektrotechniczny* **2009**, *85*, 127–132.
40. Rymarski, Z.; Bernacki, K.; Dyga, Ł.; Davari, P. Passivity-based control design methodology for UPS systems. *Energies* **2019**, *12*, 4301. [CrossRef]

41. Bernacki, K.; Rymarski, Z. Electromagnetic compatibility of voltage source inverters for uninterruptible power supply system depending on the pulse-width modulation scheme. *IET Power Electron.* **2015**, *8*, 1026–1034. [CrossRef]
42. Rymarski, Z.; Bernacki, K.; Dyga, Ł. Measuring the power conversion losses in voltage source inverters. *AEU-Int. J. Electron. Commun.* 2020, p. 153359, in press. Available online: https://doi.org/10.1016/j.aeue.2020.153359 (accessed on 17 July 2020).